

UC Irvine

UC Irvine Previously Published Works

Title

Effect of Commercial Gas Diffusion Layers on Catalyst Durability of Polymer Electrolyte Fuel Cells in Varied Cathode Gas Environment

Permalink

<https://escholarship.org/uc/item/18m4q677>

Journal

Small, 18(33)

ISSN

1613-6810

Authors

Khedekar, Kaustubh

Satjaritanun, Pongsarun

Stewart, Sarah

et al.

Publication Date

2022-08-01

DOI

10.1002/sml.202201750

Peer reviewed

Effect of Commercial Gas Diffusion Layers on Catalyst Durability of Polymer Electrolyte Fuel Cells in Varied Cathode Gas Environment

Kaustubh Khedekar, Pongsarun Satjaritanun, Sarah Stewart, Jonathan Braaten, Plamen Atanassov, Nobumichi Tamura, Lei Cheng,* Christina M. Johnston,* and Iryna V. Zenyuk*

Gas diffusion layers (GDLs) play a crucial role in heat transfer and water management of cathode catalyst layers in polymer electrolyte fuel cells (PEFCs). Thermal and water gradients can accelerate electrocatalyst degradation and therefore the selection of GDLs can have a major influence on PEFC durability. Currently, the role of GDLs in electrocatalyst degradation is poorly studied. In this study, electrocatalyst accelerated stress test studies are performed on membrane electrode assemblies (MEAs) prepared using three most commonly used GDLs. The effect of GDLs on electrocatalyst degradation is evaluated in both nitrogen (non-reactive) and air (reactive) gas environments at 100% relative humidity. In situ electrochemical characterization and extensive physical characterization is performed to understand the subtle differences in electrocatalyst degradation and correlated to the use of different GDLs. Overall, no difference is observed in the electrocatalyst degradation due to GDLs based on polarization curves at the end of life. But interestingly, MEA with a cracked microporous layer (MPL) in the GDL exhibited a higher electrocatalyst loading loss, which resulted in a lower and more heterogeneous increase in the average electrocatalyst nanoparticle size.

1. Introduction

The transportation sector generates 29% of the total U.S. greenhouse gas emissions.^[1] Only 7% of the total vehicles on road are heavy duty diesel trucks (HDDTs). But HDDTs are a source of one fourth of the total carbon dioxide (CO₂) emissions from the transportation sector.^[2] Therefore, developing a zero-emission alternative for HDDTs is of critical importance. Heavy duty trucks powered with green hydrogen using low temperature polymer electrolyte fuel cells (PEFCs) are one such promising alternative. Compared to battery electric trucks, they require low refueling time and possess excellent driving range without negatively affecting the payload capacity. However, high initial cost, availability of refueling stations, and long-term durability are limiting widespread commercialization of PEFC heavy duty trucks.

PEFCs are electrochemical devices that use hydrogen as a fuel on the anode

and air as oxidant on cathode to produce electricity and water. Figure S1, Supporting Information, shows a cross section of PEFC with the corresponding transport and reaction processes. Hydrogen flows through channels of the anode flow field and diffuses through the gas diffusion layer (GDL) into the anode catalyst layer, where it is oxidized to form protons and electrons. Protons then transport through the polymer electrolyte membrane (PEM) and electrons travel through the external circuit and recombine in the cathode catalyst layer. Oxygen from air flows through the channels of the cathode flow field, diffuses through the GDL and is reduced to form water in the cathode catalyst layer. GDLs play an important role in delivering gas and electrons, while removing heat and water. In addition, GDLs also provide mechanical integrity to the PEFCs.^[3,4] The kinetics of oxygen reduction reaction (ORR) are sluggish and platinum (Pt) electrocatalyst is utilized in PEFC stacks. For a manufacturing volume of 100 000 PEFC systems per year, more than 37% of the total stack cost comes from electrocatalyst and its applications.^[5] Thus, low Pt loading with high electrochemically active surface area (ECSA) is essential for PEFC systems to achieve cost and performance parity with combustion engines


K. Khedekar, P. Atanassov, I. V. Zenyuk
Department of Material Science and Engineering; National Fuel Cell
Research Center

University of California
Irvine, CA 92697, USA
E-mail: Iryna.zenyuk@uci.edu

P. Satjaritanun, P. Atanassov, I. V. Zenyuk
Department of Chemical and Biomolecular Engineering; National Fuel
Cell Research Center
University of California
Irvine, CA 92697, USA

S. Stewart, J. Braaten, L. Cheng, C. M. Johnston
Bosch Research and Technology Center North America
Sunnyvale, CA 94085, USA
E-mail: lei.cheng2@us.bosch.com; christina.johnston@us.bosch.com

N. Tamura
Advanced Light Source
Lawrence Berkeley National Laboratory
Berkeley, CA 94720, USA

 The ORCID identification number(s) for the author(s) of this article can be found under <https://doi.org/10.1002/smll.202201750>.

DOI: 10.1002/smll.202201750

of HDDTs. Using smaller Pt nanoparticles ($\approx 1\text{--}3$ nm) supported on carbon in the cathode catalyst layer helps achieve these targets but durability of such catalysts is significantly reduced. This negative effect on durability is caused by an increase in surface energy due to the high surface to volume ratio of nanoparticles. Therefore, it is of the utmost importance to understand electrocatalyst degradation and the effect of various MEA components on it to reduce cost without negatively affecting PEFC system performance.

Electrocatalyst degradation is a major challenge for PEFC technologies. The Pt nanoparticle surface undergoes repeated oxidation and reduction during vehicle lifetime. The repeated oxidation and reduction leads to dissolution of Pt, a primary degradation mechanism that results in the loss of ECSA loss.^[6,7] The dissolution of Pt into Pt ions leads to three subsequent ECSA loss pathways. In the first pathway, Pt ions redeposit on nearby larger Pt nanoparticles thereby increasing the Pt nanoparticle size. This is known as electrochemical Ostwald ripening.^[7,8] This happens due to the Gibbs–Thomson effect.^[9] Pourbaix diagrams of bulk Pt and Pt nanoparticles show that Pt nanoparticles are thermodynamically unstable and degrade in typical PEFC operation voltage and pH range.^[9,10] In the second pathway, dissolved Pt ions in the cathode catalyst layer diffuse through the ionomer phase towards the membrane and are reduced within the membrane near cathode catalyst layer causing Pt band formation.^[11] In the third and last ECSA loss pathway, Pt ions leave the cathode catalyst layer with the effluent water.^[12] The U.S. Department of Energy (DOE) accelerated stress test (AST) consists of square wave potential cycling (30 000 cycles) from the lower potential limit (LPL) of 0.6 V to the upper potential limit (UPL) of 0.95 V with a hold time of 3 s each. This protocol is used to simulate vehicle lifetime and study degradation mechanisms of the electrocatalyst in-depth. Previous studies^[13–15] have shown that maximum Pt dissolution occurs during the cathodic scan of the square wave potential AST cycle. Pt surface oxides are formed during the UPL hold and are subsequently reduced during the cathodic scan. Relative humidity (RH) directly affects the Pt surface oxide coverage and therefore is a critical stressor for electrocatalyst degradation. Our recent publication^[16] shows significantly larger Pt particle size at the end of life (EOL) for ASTs performed at 100% RH (absolute average value of nanoparticle size, not difference), compared to 40% RH (absolute average value of nanoparticle size). The study also highlighted heterogeneity in Pt electrocatalyst degradation due to differences in heat and water management between land–channel and inlet–outlet of the flow field. The differences affected Pt ion mobility and PtO coverage between land–channel and inlet–outlet of the flow field in both nitrogen and air cathode gas environments.

Thus far most of the durability studies have focused on Pt degradation under varied cell temperature, gas environments, gas relative humidity, flow-fields, varied UPL, and Pt loading.^[13,14,16–18] Other studies have reported beginning of life (BOL) performance of PEFCs with varied GDLs, micro porous layers (MPLs) modified with various additives or by introduction of mechanical and chemical modifications.^[19,20] However, the impact of GDLs on Pt degradation has not been studied. The GDL is a bi-layer composed of a highly porous gas

diffusion substrate (GDS) and a MPL coating made of carbon and hydrophobic additives. The typical thickness of a commercially available GDL is in the range of 100–500 μm . The GDS is a carbonaceous skeleton made up of carbon fibers arranged in different patterns and has an average porosity of 70–90% with an average pore diameter ranging from 5–40 μm .^[3] The MPL coating is made from slurry of carbon black and a hydrophobic polymer such as PTFE. Compared to GDS, MPL has a much lower porosity of 25–50% and a finer average pore diameter ranging from 50–200 nm.^[21] The GDL regulates both temperature and humidity of the cathode catalyst layer and can therefore significantly influence electrocatalyst durability.

In this study three widely used and commercially available GDLs were selected to elucidate their impact on the cathode catalyst layer degradation. The selected GDLs were designed for high RH and high current density operating conditions. The MEAs were prepared using Sigracet 22BB (22BB), Freudenberg H23C6 (H23C6), and AvCarb MB30 (MB30) as cathode GDLs. All three MEAs were first tested in the nitrogen environment AST with fixed UPL. Following this, two GDLs were down selected to be tested in an air environment AST to simulate actual PEFC operation. Advanced characterization techniques were used to spatially resolve Pt degradation between the three MEAs with different GDLs. In addition, computational fluid dynamic (CFD) simulations using Lattice Boltzmann method (LBM) were utilized to predict water distribution in the MEAs.

2. Results and Discussion

X-ray computed tomography (CT) was used to characterize morphological differences between the three GDLs studied. The cross-sectional tomograph of 22BB in **Figure 1a** shows a relatively level MPL surface with a significant presence of cracks. The in-plane images show that cracks have $\approx 10\text{--}20$ μm width. The cracks penetrate the entire thickness of the MPL and potentially provide a low-resistance pathway for the transport of reactants and products to and from the cathode catalyst layer. It can also be noticed from both the cross sectional and the in-plane grayscale images that 22BB has a MPL which is embedded in the GDS. This embedding most likely happens when the MPL slurry is casted on the GDS, and the slurry flows into the substrate before drying completely. Lastly, the images show that the GDS was made of chopped carbon fibers held together by the carbonaceous binder.

Figure 1d shows the porosity of 22BB GDL, as a function of its thickness, which is ≈ 209 μm . The MPL meso-porosities in this study were neglected and the only porosity measured was for the macroscale cracks. The cracks within MPL occupied $\approx 20\%$ of the surface area, furthermore 22B showed the MPL to be embedded into 50% of the GDS. As the embedded MPL disappeared, the porosity plateaued giving an average porosity value of 78%. A broad and bimodal distribution of pore sizes in the GDS was observed, resulting in an average pore radius of 14.7 μm for 22BB. The bimodal distribution was fit with the probability density function (PDF) of log-normal bimodal distribution, where the fitting parameters show two radii of distribution, 2.2 μm and 13.6 μm , as shown by Table S1a, Supporting Information.

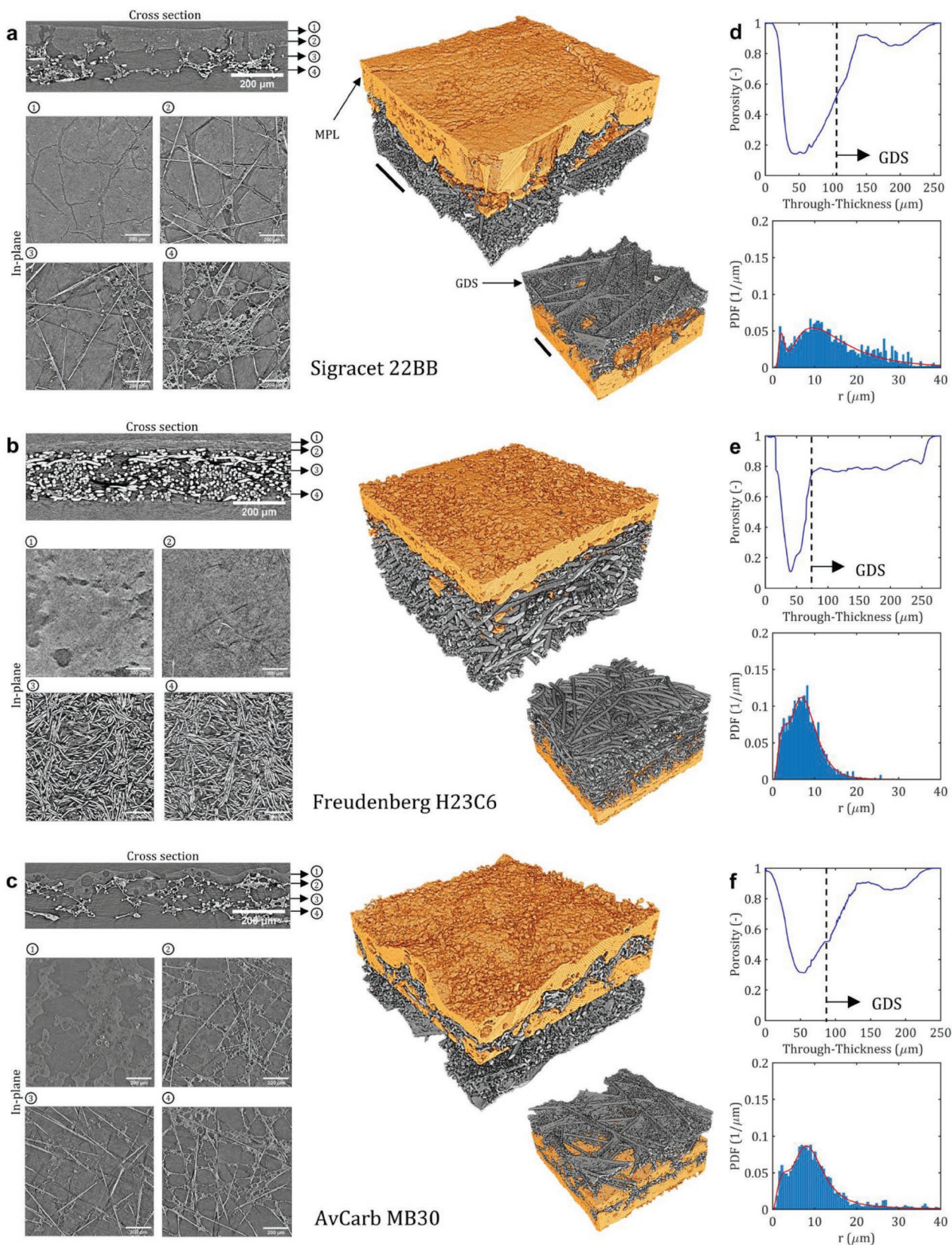


Figure 1. X-ray CT visualization and analysis of three GDLs used in this study. (Left) 2D grayscale cross-section tomographs (above) and in-plane tomographs (below). The GDLs studied are: a) 22BB, b) H23C6, and c) MB30. (Center) 3D reconstructions with MPL and GDS view. (Right) d–f) porosity as a function of GDS thickness (above) and pore size distribution (below) for 22BB, H23C6, and MB30 respectively. Scale bars, 100 μm .

Tomographic images of H23C6 in Figure 1b show a smooth and thin MPL over a GDS that is not embedded and is almost free-standing. The GDS is made of curled carbon fibers that are mechanically bound. This GDS does not have a carbonaceous binder. A sharp increase in the porosity followed by a plateau was observed for H23C6 in Figure 1e, which is indicative of the distinct transition between MPL and GDS. The average porosity of H23C6 was found to be 80%. Figure 1e also shows a narrow but bimodal pore radius distribution for the GDS of H23C6 highlighting its uniformity with an average pore radius of 7.6 μm . The probability density function (PDF) log-normal distribution fits show the radii of distribution are 4.4 and 8.4 μm , as reported by Table S1b, Supporting Information. Figure 1c shows tomographic images of MB30, which reveal a highly uneven and undulating MPL surface with presence of large pores of $\approx 5\text{--}10\ \mu\text{m}$. The voids within MPL make it highly porous. Like 22BB, MB30 also has an embedded MPL as seen in the in-plane images and 3D rendering. The GDS has fibers like 22BB but the carbonaceous binder used is highly porous. The pores in both the MPL and the binder suggest use of sacrificial material during the manufacturing to increase porosity. Figure 1f shows that MPL is much more porous compared to 22BB and H23C6 with a linear increase in porosity near MPL|GDS transition, when plotted as a function of through thickness. This is indicative that the MPL is embedded in the GDS, which can also be observed visually. The average porosity of MB30 is 83%. Figure 1f also reveals the somewhat narrow pore radius distribution of the MB30 GDS with an average pore radius of 10.9 μm . The in-plane tortuosity values were computed to be similar for three GDLs, as shown in Table 1. Bimodal log-normal fits were generated with mean radii of 3.4 and 9.6 μm as shown by Table S1c, Supporting Information. The morphology of 22BB and MB30 are somewhat similar, with similar average radii, embedded MPLs, fibers of GDS being bound by a binder. H23C6 is significantly different with smaller average pores, free-standing MPL, curled carbon fibers, and higher thickness. Table 1 summarizes values of all the critical parameters of the three selected GDLs. Figure S2, Supporting Information, shows 3D reconstructed images of 1 by 1 cm area highlighting key features of each GDL over a broader scale.

Polarization curves under differential conditions collected at 0, 1000, 5000, 15 000, and 30 000 N_2 AST cycles stage for MEA with each GDL are shown in Figure 2a–c. All the MEAs show significant voltage losses in the kinetic and mass transport regions of the polarization curves over the course of the AST. This loss in voltage for each GDL can be associated with coarsening of Pt nanoparticles resulting in the loss of ECSA. For all the MEAs, voltage loss within the first 5000 AST cycles is

mostly kinetic and is dominated by decrease in the ECSA, since the slope of the polarization curve does not change. After 15 000 cycles, a change of slope in the polarization curve is evident. No significant change in the high frequency resistance (HFR) suggests that this change in slope could be due to increase in the oxygen mass transport resistance or loss of ionic conductivity in the cathode catalyst layer, both of which will be discussed in the next section. A direct comparison of before and after AST polarization curves from the three MEAs were plotted as in Figure 2d. For each GDL MEA, identical cell voltages were recorded in the kinetic region at the BOL, which is expected as GDL should not impact the kinetic region at low geometric current densities. Different GDLs can result in different HFR due to inadequate and uneven compression leading to differences in ohmic overpotentials. But care was taken in this study to achieve optimum GDL compression with the lowest possible HFR value for each GDL. As a result, 22BB, H23C6 and MB30 all showed negligible differences in HFR, with values in the range of 85–95 $\text{m}\Omega\ \text{cm}^2$. This also eliminated any undesired catalyst degradation caused due to suboptimal settings and allowed a fair comparison of polarizations before, during, and after AST. The effect of GDL emerges in the mass transport region. At the BOL, 22BB shows the lowest overpotential followed by H23C6 and MB30 at 1, 1.5, and 2 $\text{A}\ \text{cm}^{-2}$. This can be credited to the MPL cracks of 22BB, which facilitated better removal of produced water and prevented water accumulation in the cathode catalyst layer at high current densities. After AST, no significant difference was observed in the kinetic and ohmic regions of the polarization curves suggesting catalyst degradation led to identical ECSA loss for all three nitrogen environment ASTs. The improved overpotential in the mass transport region of 22BB carried throughout the N_2 AST, when compared to H23C6 and MB30. This also underlined the potential effectiveness of cracks as a strategy to improve MEA performance in the mass transport region.

For MEAs with three different GDLs, the ECSA during nitrogen environment ASTs was plotted as a function of the number of AST cycles in Figure 3a. The ECSA was calculated by integrating the hydrogen underpotential deposition region (0.1–0.4 V) from cyclic voltammograms (CVs) collected in hydrogen/nitrogen (anode/cathode) under atmospheric pressure (see Figure S3, Supporting Information). Before the nitrogen environment AST, 22BB, H23C6 and MB30 showed initial ECSA values of 35.42, 33.1 and 34.6 $\text{m}^2\ \text{g}^{-1}$, respectively. Minimal differences observed in the initial ECSA values are from sample-to-sample variation. Approximately 50% of the initial ECSA value was lost by all the GDLs within the first 5000 cycles of the nitrogen environment AST (i.e., within 16% of the total AST duration). After AST, ECSA values for 22BB, H23C6 and MB30 were 6.50, 7.50 and 6.53 $\text{m}^2\ \text{g}^{-1}$ respectively, resulting in a total loss of $\approx 78\%$ of the initial ECSA value for all the GDLs. No differences were observed in the ECSA loss trend between the three MEAs with different GDLs, although a very small difference can be noted in the after AST normalized ECSA plot (inset Figure 3a) with 22BB and MB30 showing the lowest values. The ECSA loss corresponds well with the almost identical increase in kinetic overpotentials observed in the air polarization curves. The loss in the ECSA is dominated by increase in the Pt nanoparticle size due to electrochemical

Table 1. GDL properties for SGL 22BB, H23C6, and AvCarb MB30.

Parameters	Sigracet 22BB	Freudenberg H23C6	AvCarb MB30	Unit
Total thickness	209 \pm 9	226 \pm 6	182 \pm 7	μm
Micro porous layer thickness	74 \pm 7	35 \pm 3	41 \pm 9	μm
Porosity	78%	80%	83%	–
In-plane tortuosity	1.21	1.26	1.31	–
Average pore radius, r_{ave}	14.7	7.6	10.9	μm

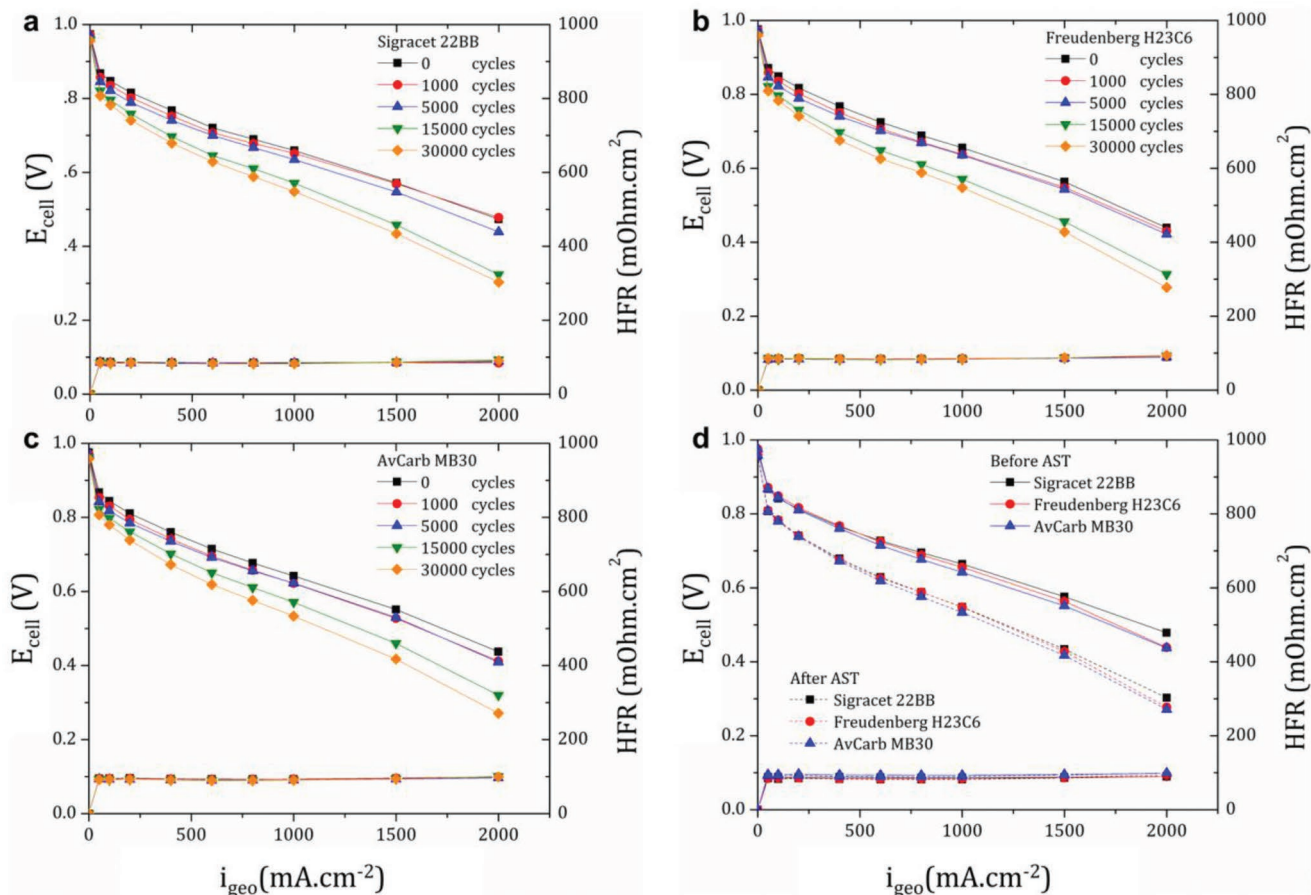


Figure 2. Polarization curves collected at BOL, 1000, 5000, 15 000, and 30 000 AST cycles in differential conditions at 80 °C in 100% RH under 150 kPa (a) pressure. a) 22BB. b) H23C6. c) MB30 and d) before versus after AST. The high-frequency resistance (HFR) is plotted on the right-side y-axis.

Ostwald ripening followed by Pt band formation near the membrane/cathode interface or via effluent water. Figure 3b shows pressure independent oxygen mass transport resistance (R_{PI}) as a function of decreasing roughness factor (rf) as the AST progresses. After 5000 cycles apparent increase in the R_{PI} can be noticed as the rf decreases below the threshold of ≈ 40 . This apparent increase in the R_{PI} can lead to the evolution of mass transport overpotentials at current densities as low as 0.5 A cm^{-2} and cause change in the slope of the ohmic region as observed in air polarization curves of the three GDLs. Oxygen mass transport resistance at the Pt-ionomer interface ($R_{PtO_2}^{Pt}$) after AST, given by the slope of total oxygen mass transport resistance (R_{total}) versus rf^{-1} at different total pressures^[22] (see Figure S4, Supporting Information) was averaged and is shown in Figure 3c for all three GDLs. At 160 kPa, 22BB shows a value of $\approx 3.5 \text{ s cm}^{-1}$ while H23C6 and MB30 show values close to ≈ 2.1 and 2.3 s cm^{-1} , respectively. This means that a higher contribution from $R_{PtO_2}^{Pt}$ in R_{PI} is seen for 22BB suggesting either less contact between ionomer and the Pt catalyst due to particle size increase and/or decreased average Pt loading compared to H23C6 and MB30. Ionomer conductivity in the catalyst layer was plotted as a function of the number of AST cycles in Figure 3d. The conductivity was calculated by fitting the EIS measured in hydrogen/nitrogen (anode/cathode)

at 0.2 V (see Nyquist plots in Figure S5, Supporting Information). A small increase in the conductivity is noticed in the first 5000 cycles for all the GDLs. Therefore, ionic conductivity is not responsible for the slope increase in the polarization curves observed in Figure 2. Mass activity calculated from Tafel plots (see Figure S6, Supporting Information) is shown in Figure 3e. All the GDLs showed a Tafel slope close to the theoretical value of $\approx 70 \text{ mV dec}^{-1}$. The trend of mass activity loss agrees well with the loss of ECSA. No significant change in the Tafel slope was observed before and after the nitrogen environment AST. An average of $\approx 78\%$ of initial mass activity was lost by all the GDLs after AST failing to achieve the DOE target of less than 40% loss of initial mass activity. Lastly, Figure 3f shows voltage loss trend at 0.8 A cm^{-2} for each GDL over the course of the AST. There are identical voltage losses for all the GDLs at each stage of the AST with none of them meeting the DOE voltage loss target of less than 40 mV of the initial value. Approximately 100 mV of voltage loss was observed at 0.8 A cm^{-2} for each MEA. To summarize, the electrochemical characterization results show no difference in the degradation of MEAs having 22BB, H23C6, and MB30 GDLs in nitrogen environment ASTs at 100% RH. This suggests that the Pt oxide coverage, which is the primary degradation stressor, remains unaffected by significant differences in GDL morphology at 100% RH in a

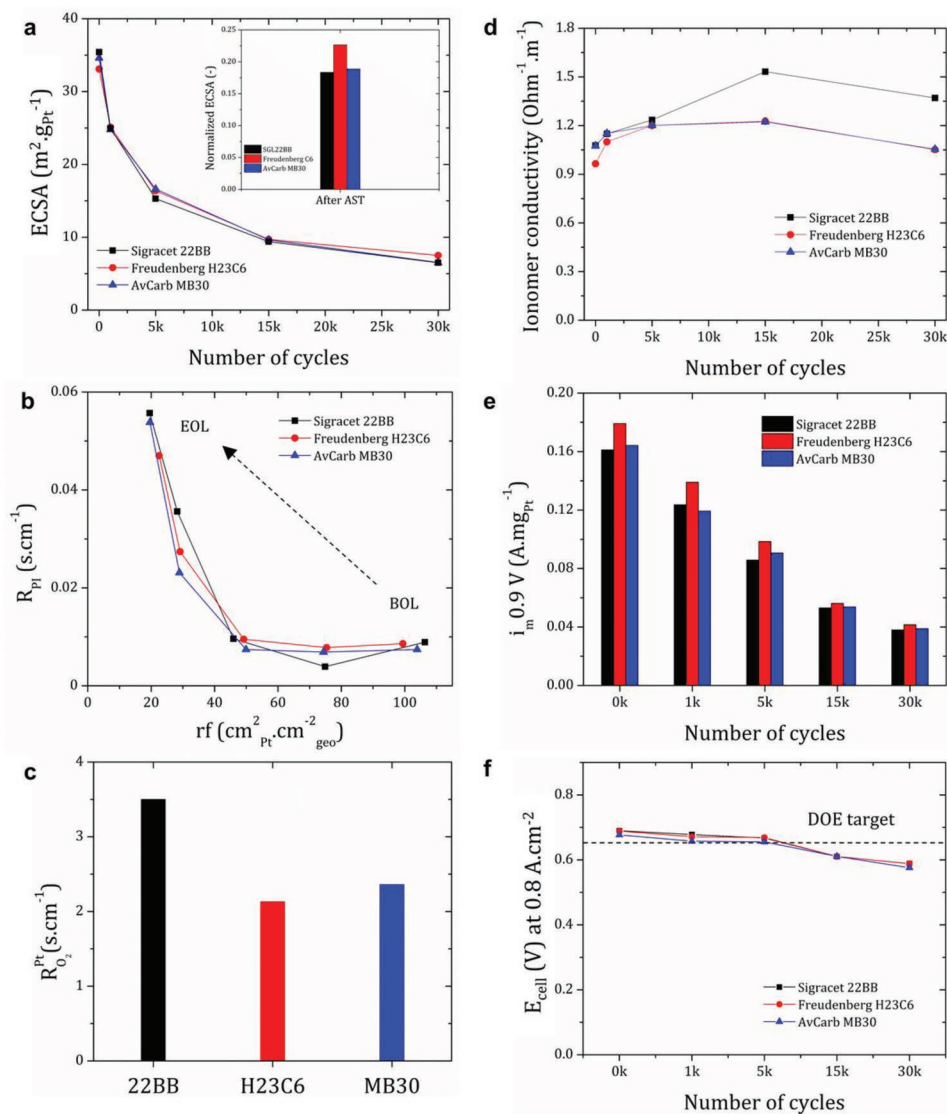


Figure 3. Electrochemical characterization for MEAs having 22BB, H23C6, MB30 GDLs. a) ECSA loss as a function of number of AST cycles. b) Pressure independent oxygen mass transport resistance as a function of decreasing rf . c) Average oxygen mass transport resistance at the Pt-ionomer interface during nitrogen AST. d) Ionomer conductivity as a function of number of AST cycles. e) Mass activity calculated at 0.9 V from Tafel plots generated from polarization data collected in oxygen environment plotted as function of number of AST cycles. f) Voltage loss at 0.8 $\text{A} \cdot \text{cm}^{-2}$ as a function of number of AST cycles.

non-reactive environment with an absence of electrochemically produced water. This can be attributed to Kelvin effect, where the incoming water vapor will condense on the surface of Pt nanoparticles causing insignificant differences of Pt oxide coverage within the cathode catalyst layers having different GDLs.

Active area (4 cm^2) of each GDL was mapped before and after the nitrogen environment AST using micro X-ray diffraction (micro XRD) and micro X-ray fluorescence (micro XRF) techniques to study the Pt nanoparticle size growth and Pt mass loading changes. **Figure 4a** shows the 2 by 2 cm mapped area with respect to the 5 cm^2 flow field used. **Figure 4b–e** shows micro XRD maps (above) and normalized micro XRF maps (below) for control, 22BB, H23C6, and MB30 respectively. An average Pt nanoparticle size of $2.69 \pm 0.10 \text{ nm}$ can be observed for the control sample (i.e., before AST). An average Pt

nanoparticle size of $9.08 \text{ nm} \pm 0.86 \text{ nm}$ was observed for 22BB while an average Pt nanoparticle size of $9.11 \text{ nm} \pm 0.82 \text{ nm}$ and $9.26 \text{ nm} \pm 1.54 \text{ nm}$ was observed for H23C6 and MB30, respectively. All the MEAs showed a significant increase in the Pt nanoparticle size after nitrogen AST, resulting from electrochemical Ostwald ripening mechanism. Somewhat similar distribution of Pt nanoparticle size in the 2D mapping is observed for 22BB, H23C6, and MB30. Generally, a larger nanoparticle size area is located at the first 90° bend, near inlet, of the serpentine flow field. In H23C6, the larger nanoparticle size area extends further to the next 90° bend, compared to 22BB and MB30. Even though all the three MEAs show heterogeneity with a greater increase in Pt nanoparticle size closer to the inlet, some degree of heterogeneity can be observed for the MEA having 22BB compared to H23C6 and MB30. To further understand this degradation

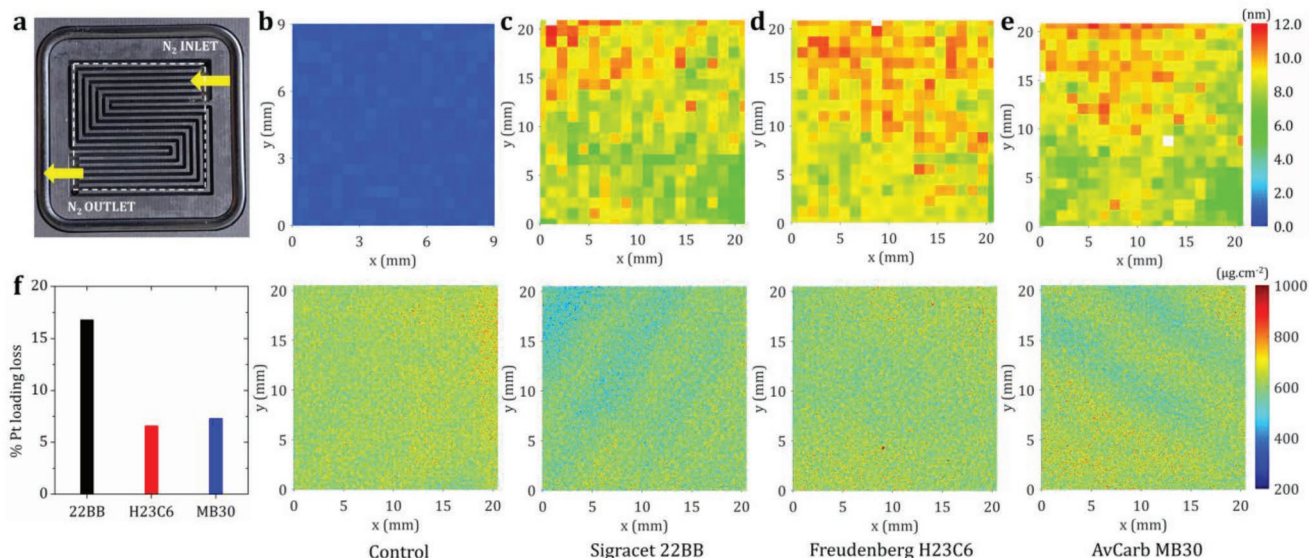


Figure 4. Analysis of Pt nanoparticle size and Pt loading for MEAs with 22BB, H23C6, and MB30 as cathode GDLs after nitrogen AST. a) Mapped area of the flow field with inlet and outlet marked. b–e) (Above) micro X-ray diffraction maps and (below) micro X-ray fluorescence maps. f) Percentage of average Pt loading loss for each GDL MEA after nitrogen environment AST.

heterogeneity, micro XRF maps were analyzed and quantified. An average Pt loading of $601 \mu\text{g cm}^{-2}$ was seen for the control sample, which is a summation of the anode and cathode Pt loadings. All the GDLs showed some amount of Pt loading loss from the cathode catalyst layers' loadings evident from the micro XRF maps normalized using control sample loading (to eliminate sample to sample variation and clearly understand the effect of GDLs). Like the micro XRD maps, a difference in average Pt loading after AST (see Table S2, Supporting Information) was clearly noticed between the three MEAs with 22BB showing the lowest average Pt loading. Figure 4f shows MEA with 22BB having $\approx 16\%$ loss of initial Pt loading, which is more than twice that when compared to H23C6 and MB30 that show a Pt loading loss of $\approx 6\text{--}7\%$. This also indicates that separate ECSA loss pathways may have been followed by the different GDL MEAs to reach similarity after AST ECSAs.

The understanding of GDL morphology from the micro X-ray CT data suggests that this difference in Pt nanoparticle size increase and average Pt loading loss between MEAs having 22BB versus H23C6 and MB30 could be related to the presence of MPL cracks in 22BB. The presence of MPL cracks can result in a higher flux of liquid water from the cathode catalyst layer. Therefore, a much larger fraction of the Pt ions have a high probability of leaving the cathode catalyst layer through effluent water. This explains the lower increase in average Pt nanoparticle size and decrease in average Pt loading (after AST in 22BB) as a lower fraction of Pt ions are available for redeposition on nearby larger nanoparticles. Previously, an operando small angle X-ray scattering study has shown significant loss of Pt loading in flowing conditions when compared to stagnant conditions.^[23] In addition to this, multiple studies have reported such heterogeneity in Pt nanoparticle size increase (between inlet–outlet and land–channel)^[16,17] and loss or change in cathode catalyst layer Pt loading,^[24] which can be explained through differences in liquid water flux.

To confirm the average Pt loading loss trend and solidify that Pt oxide coverage and hence degradation at 100% RH will not be affected by electrochemically produced water (due to Kelvin effect), MEAs were subjected to AST in air environment on the cathode. GDLs 22BB and H23C6 were selected as they display a significant difference between their morphologies. Figure 5 shows the before and after air AST electrochemical characterization. Like nitrogen environment ASTs, no difference is observed in the polarization curves in Figure 5a between the two MEAs after degradation. The voltage loss at 0.8 A cm^{-2} is $\approx 50 \text{ mV}$ which is half of that seen in the nitrogen environment. The average Pt nanoparticle size after air AST for both the GDLs was $\approx 3.90 \pm 0.31 \text{ nm}$, which is also significantly lower compared to nitrogen ASTs. This difference between particle size in N_2 AST and air AST is primarily due to the decreasing UPL limit during voltage cycling in case of air ASTs (as UPL is set to be OCV in air AST case) highlighted by Figure S7b,c, Supporting Information. Figure S7c, Supporting Information, also shows that the voltage cycling profile experienced by both the GDLs over the course of AST was similar. Figure 5b shows Tafel plots before and after AST with little to no difference between the two MEAs after degradation. The Tafel slope shows minimal change, as well. Therefore, the calculated mass activity at 0.9 V plotted in Figure 5d is similar after degradation. A loss of $\approx 60\%$ of initial mass activity was observed. Figure 5c shows initial ECSA values of 29.8 and $28.9 \text{ m}^2 \text{ g}^{-1}$ for 22BB and H23C6, respectively. This slightly lower ECSA values for the air AST MEAs are from batch to batch variation. Almost 50% of initial ECSA was lost after the air AST. Therefore, it can be confirmed that, like nitrogen ASTs, no difference in electrochemical performance was noted after degradation in air ASTs for 22BB and H23C6. Figure S8, Supporting Information, shows additional electrochemical characterization while Figure S9, Supporting Information, shows micro XRF maps of control sample along with 22BB and H23C6 after air AST. A similar

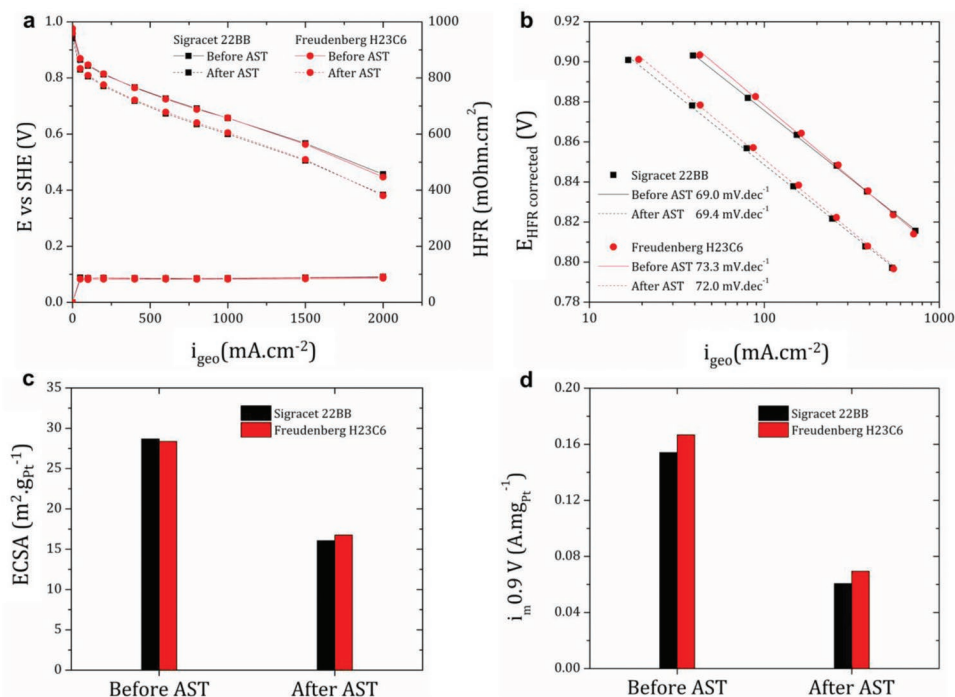


Figure 5. Electrochemical characterization of MEAs with 22BB and H23C6 as cathode GDLs subjected to air AST. a) Before versus after AST differential polarization curves collected at 80 °C in 100% RH under 150 kPa (a) pressure. b) Before versus after AST Tafel plots generated from polarization data collected in oxygen environment. c) Before versus after AST ECSA. d) Before versus after AST mass activity calculated from Tafel plots at 0.9 V.

difference of average Pt loading loss can be seen between MEAs having 22BB (7.5%) and H23C6 (3.7%) GDLs after air AST. The overall percentage of loading loss has decreased for both MEAs due to decreasing UPL, but the difference caused due to the GDLs has stayed constant.

CFD simulations using LBM were performed to simulate water transport through the GDLs. X-ray CT images were used as simulation domains. **Figure 6a–c** shows 3D reconstructions of 22BB, H23C6, and MB30 with simulated flow of liquid water through the GDLs (above) along with 2D colormap cross sections of liquid water saturation (below). Water was injected at the bottom of the MPL, to simulate liquid water formation (electrochemically produced or condensed) in the cathode catalyst layer and transport through the MPL. After injection, liquid water starts building up pressure to escape through the hydrophobic pores of the MPL. In the case of 22BB the breakthrough pressure was found to be at 8.5 kPa. This low value is due to the presence of MPL cracks, as they provide a low pressure preferential pathway for water to escape. This can be seen from the breakthrough pressure difference between 22BB versus H23C6 and MB30 in **Figure 6d**. A breakthrough pressure of 8.5 kPa was observed for 22BB while 12.8 and 21.9 kPa pressures were observed for H23C6 and MB30, respectively. **Table S4**, Supporting Information, contains stagnation pressure for each GDL. All the data confirms a higher flux of liquid water in the cathode catalyst layer with 22BB as the GDL compared to H23C6 and MB30. This results in a loss of dissolved Pt ions from the cathode catalyst layer via effluent water as confirmed by the micro XRF maps previously. Average liquid water saturation inside GDS was observed to be highest for 22BB (24%) resulting in better liquid water removal from the cathode

catalyst layer due to MPL cracks. H23C6 and MB30 show much lower liquid water saturation of 7% and 13%, respectively resulting in low liquid water flux.

3. Conclusion

Catalyst ASTs were performed on MEAs using commercially available GDLs Sigracet 22BB, Freudenberg H23C6, and AvCarb MB30 in both nitrogen and air environments. Micro X-ray computed tomography was performed on each GDL to analyze differences in morphological properties such as thickness, porosity, pore size distribution, and to also identify critical features. Thorough in situ electrochemical characterization was performed at various stages of the ASTs to better understand the degradation phenomena. Micro XRD mapping was used to analyze the increase in average Pt nanoparticle size while micro XRF mapping was used to quantify average Pt loading after ASTs. CFD simulations using LBM were performed on water injection micro X-ray computed tomography data collected for each GDL to understand liquid water saturation/flux and breakthrough pressure.

From micro X-ray CT, the embedded nature of MPLs in 22BB and MB30 was detected while H23C6 showed a free standing MPL. MPL thicknesses of 74 ± 7 , 35 ± 3 and 41 ± 9 μm were observed for 22BB, H23C6 and MB30, respectively. MPL of 22BB showed cracks, which resulted in better water management confirmed by slightly better electrochemical performance in the mass transport region. The cracks provided a direct pathway for the removal of liquid water from the cathode catalyst layer. An ECSA loss of 78% and 60% was observed after nitrogen and air

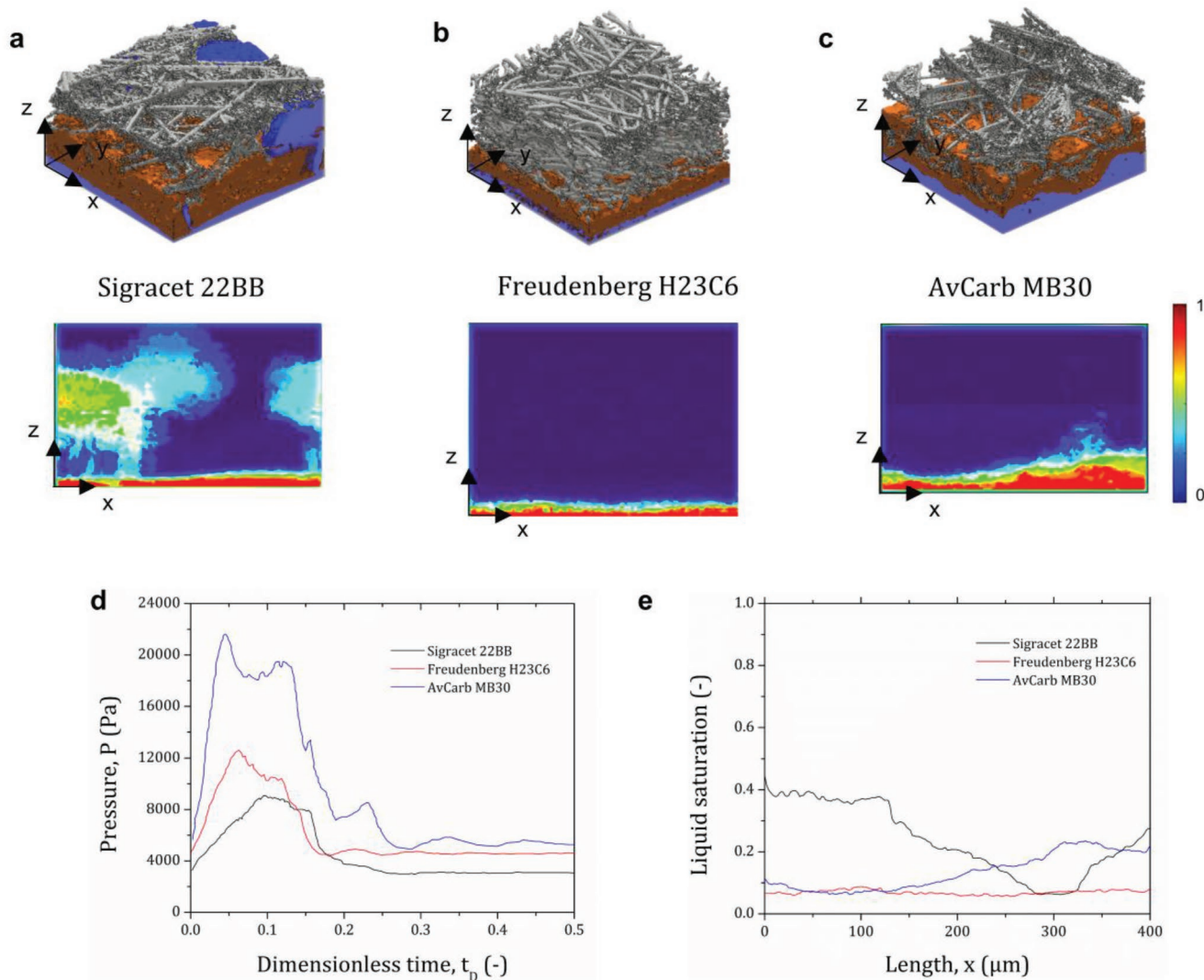


Figure 6. LBM simulations of water transport through the GDLs. a–c) (Above) 3D reconstructions of liquid water saturation simulation, (below) 2D colormaps of liquid water saturation. d) Breakthrough pressure as function of time. e) Liquid water saturation as a function of length.

ASTs, respectively, for each MEA. A voltage loss of 100 mV (DOE target 40 mV) was observed in the air polarization curves after the nitrogen ASTs of each GDL. Close to 50% of initial ECSA and 47% of initial mass activity was lost within the first 5000 AST cycles by all the MEAs. Although some differences were observed in the mass transport region before and after AST (due to significantly different GDL morphologies), no difference was observed in electrocatalyst degradation (arising due to differences in GDLs) from electrochemical performance. Micro XRD maps showed an increase in the average Pt nanoparticle size for all GDL MEAs, which correlated with the ECSA loss data. The MEA with 22BB as cathode GDL showed a much higher degree of heterogeneous Pt nanoparticle size growth with a lower average Pt nanoparticle size after nitrogen AST. Micro XRF maps also showed almost 16% of average Pt loading loss for 22BB compared to 6–7% average Pt loading loss for H23C6 and MB30.

CFD simulations using LBM showed that 22BB had the lowest breakthrough (8.5 kPa) and stagnation pressure (3.7 kPa) coupled with the highest (24%) liquid water saturation compared

to H23C6 and MB30. A combined analysis of micro XCT, micro XRD, micro XRF, and CFD simulation suggests that higher liquid water flux due to presence of MPL cracks in 22BB results in more direct loss of dissolved Pt ions from the cathode catalyst layer. This also suggests that different pathways were taken by the three GDL MEAs to reach a similar ECSA loss.

Although the electrochemical difference cannot be observed for 30 000 AST cycles (light duty vehicle lifetime) it may show up after 90 000 AST cycles (currently being discussed to simulate heavy duty vehicle lifetime) and in dry operating conditions. The direct loss of dissolved Pt from the system is also critical in terms of Pt recycling. The study highlights the importance of designing GDLs with end-of-life performance target.

4. Experimental Section

Materials and Method: The CCMs were purchased from Ion Power Inc., New Castle, Delaware. 6 cm² active area MEAs was used by

masking 25 cm² Ion Power CCMs with Pt/C (TEC10E50E) catalyst. The Pt loading was 300 μg cm⁻² on both anode and cathode. The ionomer to carbon (I/C) ratio was 1. The CCMs had ≈27.5 μm thick Nafion XL membrane. Sigracet 22BB, Freudenberg H23C6 and AvCarb MB30 were purchased from Fuel Cell Store, College Station, Texas, USA, and were used as the three cathode GDLs. Sigracet 22BB was the anode GDL and was kept constant for all the ASTs. Additional details about the GDL properties, as specified by manufacturer and measured in laboratory can be found in Table 1 and Table S1, Supporting Information.

Testing Equipment: Fuel cell quick connect fixture (qCf) in combination with a cell fixture (cF) from balticFuelCells GmbH, Hagenower Str.73.D-19061 Schwerin, Germany was used. The flow-field contained 7× channel serpentine flow field of 6 cm² area, adapted from Simon et al.^[25] The cell compression in this setup is pneumatically controlled. A pneumatic compression pressure of ≈0.9 bar was used to achieve the manufacturer recommended 1–1.1 MPa pressure on the GDLs as shown by Figure S10, Supporting Information. This compression pressure resulted in a low contact resistance. The GDL compression was 20–22% as recommended by the different GDL manufacturers. ASTs in air environment, polarization curves, mass activity and oxygen mass transport measurements were performed using an 850e fuel cell test system with a maximum current load of 100A, while electrochemical impedance spectroscopy (EIS) in air environment was performed using an 881 Frequency Response Analyzer accessory, both from Scribner Associates, Southern Pines, North Carolina. ASTs in nitrogen environment, cyclic voltammograms, linear sweep voltammograms (LSV), and EIS in nitrogen environment were performed using Interface 5000 potentiostat from Gamry Instruments, Warminster, Pennsylvania.

Accelerated Stress Tests: The ASTs were conducted at 80 °C cell temperature in 100% RH under atmospheric pressure. Three ASTs with different cathode GDLs (22BB, H23C6 and MB30) were conducted in hydrogen/nitrogen (anode/cathode) environment while the rest of the ASTs two (22BB and H23C6) were conducted in hydrogen/air environment. ASTs were repeated to ensure reproducible performance and confirm observations. Figure S7b, Supporting Information, shows the voltage cycling profile for the nitrogen environment ASTs comprising 0.6 V lower potential limit (LPL) and 0.95 V of UPL with a dwell time of 3 s at each potential. Figure S7c, Supporting Information, shows the voltage cycling profile for the air environment ASTs with OCV as the UPL. Gas flow rates of 0.2 slpm/0.2 slpm were used for both environment ASTs for cathode and anode gases, respectively. During the ASTs, each MEA was characterized after 0, 1000, 5000, 15 000, and 30 000 AST cycles as shown by Figure S7a, Supporting Information.

Electrochemical Characterization: Cyclic voltammogram (CV), LSV, and EIS were all collected in hydrogen/nitrogen environment at 80 °C in 100% RH under atmospheric conditions with gas flow rates of 1 slpm/1 slpm on the anode/cathode, respectively. CVs were collected with a potential sweep from 0.1 to 1.2 V at a scan rate of 100 mV s⁻¹ while LSVs were collected from 0.05 to 0.8 V at scan rate of 1 mV s⁻¹ to measure hydrogen crossover. EIS was measured at 0.2 V from 20 kHz to 0.1 Hz with 6 points per decade. Voltage break-in was performed at 80C in 100% RH under atmospheric pressure by cycling the voltage between 0.8, 0.6, and 0.3 V (30 s each) for 200 cycles in a hydrogen /air environment. Voltage recovery consisted of voltage hold at 0.2 V for 1 h at 40 °C in 150% RH under 150 kPa in a hydrogen/air environment. Polarization curves in hydrogen/air and hydrogen/oxygen environments were collected in differential conditions at 80 °C in 100% RH under 150 kPa absolute pressure with gas flow rates of 1 slpm/2.5 slpm at anode/cathode, respectively. For air, 4 min holds from high current density (2 A cm⁻²) to low current density (0 A cm⁻²) were performed while for oxygen the holds consisted of 3 min from 0.75 V to OCV with increments of 25 mV. Average of the last minute was used to generate polarization curve (air) and Tafel plot (oxygen). Limiting current measurements were done by holding potential from 0.3 to 0.06 V using 0.5%, 1% and 1.5% concentrations of oxygen (balance nitrogen) at 80 °C in 75% RH under 120, 160 and 200 kPa of absolute pressures with flow rates of 1 slpm/5 slpm at anode/cathode, respectively. The measured limiting current was then used to calculate the total oxygen mass transport

resistance, pressure independent mass transport resistance, and mass transport resistance at the Pt ionomer interface based on procedures reported by Baker et al.^[26] and Greszler et al.^[22] For detailed summary of each electrochemical characterization protocol and the ASTs see Table S4, Supporting Information. Figure S7a, Supporting Information, also gives the chronology of the electrochemical experiments.

Micro X-Ray Computed Tomography: Ex-situ micro X-ray computed tomography (CT) of MEAs was performed at Beamline 8.3.2 at Advanced Light Source (ALS) at Lawrence Berkeley National Laboratory (LBNL), Berkeley, California using 25 keV energy monochromatic X-rays. 50 μm LuAg:Ce scintillator, 10× lenses, and sCMOS PCO.Edge camera were used to achieve an image with 0.65 μm pix⁻¹. Exposure time of 200 ms was used to collect 1300 images per scan. A 3D image stack was reconstructed using 2D radiographs collected from 0° to 180° rotations. The Gridrec algorithm was used within TomoPy, open-source software to perform reconstructions. The reconstruction parameters were described in detail previously.^[27,28] Open-source Fiji/ImageJ software was used for image processing and 8-bit conversion.^[29] Dragonfly, Object Research Systems was used for 3D rendering.

Computational Fluid Dynamics Simulation with Lattice Boltzmann Method: The LBM is a CFDs technique for solving a wide variety of fluid flow problems in the complex structure of the porous medium. LBM was performed to simulate the liquid water injection inside the detailed structure of GDL samples. The model utilized free surface conditions and a time-dependent simulation was used to capture the behavior of liquid water transport inside the GDL samples. XFlow 2020× (Build 102.03), which is a commercial CFD program that has a built-in LBM solver, was used to perform numerical simulations. The lattice element size was 0.65 μm, giving a total number of 18 312 548 to 22 353 320 elements, depending on the size and resolution of the computed geometry. The computational domain has a size of 400 × 400 μm² with the thickness depending on the sample. The time step was set to 0.1 μs. The liquid-water was injected under the sample at the same locations and flow rate at 1e-4 kg s⁻¹. The surface tension of liquid-water was set to 0.072 N m⁻¹, which corresponds to the surface tension of water in contact with air at 25 °C. Surface tension is also responsible for the contact angle (θ) where a surface meets a GDL surface. This is determined by the interactions across the fluid–fluid and fluid–solid interface. The GDL contact angle in the simulation was assumed to be constant and uniform at 110°.

Micro X-Ray Diffraction: Post-mortem synchrotron X-ray micro-diffraction mapping was conducted at Beamline 12.3.2 of the ALS at LBNL. A monochromatic X-ray beam of 10 keV was focused to ≈2 × 5 μm² by Kirkpatrick–Baez mirrors. The MEAs after AST were mounted on a 25° (relative to the incident beam) tilted x–y scan stage. Diffraction images were recorded with a 2D Pilatus-1 m detector mounted at 60° to the incoming X-rays in reflection mode. The detector was located ≈150 mm away from the probe spot. An exposure time of 10 s at each position was used. Calibrations for distance, center channel position, and tilt of the detector were performed based on a powder pattern obtained from a reference Al₂O₃ particles taken at the same geometry. For mapping/imaging of the 2 cm × 2 cm area of each MEA sample a scan of 20 × 20 (total 400) points was performed with a step size of 1 mm on both the x-axis and y-axis. The X-ray scan diffraction data was then processed by XMAS.^[30] Integration of the diffraction rings performed along the azimuthal direction and the peak width was determined by fitting a 2D Lorentzian function with an angular resolution of ≈0.02°. Instrumental broadening was estimated using large Al₂O₃ crystals powder in the exact same detector configuration. The estimated Pt particle size is an average from both the cathode and anode catalyst for each measured location since the synchrotron X-ray penetrates both cathode and anode. In this diffraction measurement, change of Pt particle size before and after ASTs is dominated by the cathode Pt nanoparticle size increase, as minimal/no nanoparticle size increase is expected on the anode as it was fixed at 0.0 V versus R.H.E in pure H₂ environment throughout the entire AST. Additional details about the technique have been reported earlier.^[31]

Micro X-Ray Fluorescence: Ex-situ X-ray fluorescence measurements were performed using the XGT-9000 Horiba XRF microscope. A 10 μm capillary was utilized to map an area of 20.5 mm \times 20.5 mm (4 cm²) with a resolution of 1024 px in both x and y directions giving a pixel size of 20 μm \times 20 μm . The X-ray energy was set to 50 keV. The quantified average Pt loading includes both anode and cathode as the X-ray penetrates the full MEA and reflected X-ray signal to the detector includes Pt contribution from anode and cathode. 2D colormaps were generated in MATLAB using mapped fluorescence images from the microscope. Average Pt loading was quantified for each map using a calibration curve generated from 10 μm capillary maps of calibration samples with known Pt loading. For Pt loading quantification L alpha peak of Pt was used. The average loading for each sample was reconfirmed by collecting spectrum using 1.2 mm capillary at multiple spots.

Supporting Information

Supporting Information is available from the Wiley Online Library or from the author.

Acknowledgements

3D X-ray tomography images for this paper were generated using Dragonfly software, Version 3.6. Object Research Systems (ORS) Inc., Montreal, Canada, 2018; software available at <http://www.theobjects.com/dragonfly>. The Advanced Light Source is supported by the Director, Office of Science, Office of Basic Energy Sciences, of the U.S. Department of Energy under Contract No. DE-AC02-05CH11231. The authors thank Dr. Dula Parkinson for the beamline support.

Conflict of Interest

The authors declare no conflict of interest.

Author Contributions

L.C., C.M.J., and I.V.Z. provided experimental design guidance and direction. K.K. carried out the electrochemical measurements, ASTs, XRFs, and analyzed the data. L.C. performed synchrotron XRD and analyzed data. I.V.Z. performed the synchrotron X-ray tomography experiments, P.S. analyzed the X-ray CT data and performed LBM modeling. K.K. wrote the first draft of manuscript, and all authors edited the manuscript.

Data Availability Statement

The data that support the findings of this study are available from the corresponding author upon reasonable request.

Keywords

catalyst degradation, gas diffusion layers, hydrogen, polymer electrolyte fuel cells

Received: March 19, 2022
Revised: July 4, 2022
Published online: July 24, 2022

- [1] EPA (2022) Inventory of U.S. Greenhouse Gas Emissions and Sinks: 1990-2020, U.S. Environmental Protection Agency, EPA 430-R-22-003.
- [2] D. Cook, UCS, *Engines for Change*, 2015, www.ucsusa.org/enginesforchange.
- [3] I. V. Zenyuk, D. Y. Parkinson, L. G. Connolly, A. Z. Weber, *J. Power Sources* 2016, 328, 364.
- [4] A. Forner-Cuenca, *Doctoral Thesis*, ETH Zürich, 2017.
- [5] A. Wilson, G. Kleen, D. Papageorgopoulos, U.S. Department of Energy and Fuel Cells Program, "Record 17007 Fuel Cell System Cost - 2017".
- [6] R. Borup, J. Meyers, B. Pivovar, Y. S. Kim, R. Mukundan, N. Garland, D. Myers, M. Wilson, F. Garzon, D. Wood, P. Zelenay, K. More, K. Stroh, T. Zawodzinski, J. Boncella, J. E. McGrath, M. Inaba, K. Miyatake, M. Hori, K. Ota, Z. Ogumi, S. Miyata, A. Nishikata, Z. Siroma, Y. Uchimoto, K. Yasuda, K. Kimijima, N. Iwashita, *Chem. Rev.* 2007, 107, 3904.
- [7] G. S. Harzer, J. N. Schwämmlein, A. M. Damjanović, S. Ghosh, H. A. Gasteiger, *J. Electrochem. Soc.* 2018, 165, F3118.
- [8] J. C. Meier, C. Galeano, I. Katsounaros, J. Witte, H. J. Bongard, A. A. Topalov, C. Baldizzone, S. Mezzavilla, F. Schuth, K. J. J. Mayrhofer, *Beilstein J. Nanotechnol.* 2014, 5, 44.
- [9] S. Cherevko, N. Kulyk, K. J. J. Mayrhofer, *Nano Energy* 2016, 29, 275.
- [10] S. Mitsushima, Y. Koizumi, S. Uzuka, K. I. Ota, *Electrochim. Acta* 2008, 54, 455.
- [11] S. Kundu, M. Cimenti, S. Lee, D. Bessarabov, *Membr. Technol.* 2009, 2009, 7.
- [12] J. Xie, D. L. Wood, K. L. More, P. Atanassov, R. L. Borup, *J. Electrochem. Soc.* 2005, 152, A104.
- [13] A. Kneer, N. Wagner, C. Sadeler, A.-C. Scherzer, D. Gerteisen, *J. Electrochem. Soc.* 2018, 165, F805.
- [14] H. Zhang, H. Haas, J. Hu, S. Kundu, M. Davis, C. Chuy, *J. Electrochem. Soc.* 2013, 160, F840.
- [15] M. Uchimura, S. S. Kocha, *ECS Trans.* 2007, 11, 1215.
- [16] K. Khedekar, M. R. Talarposhti, M. M. Besli, S. Kupan, A. Perego, Y. Chen, M. Metzger, S. Stewart, P. Atanassov, N. Tamura, N. Craig, L. Cheng, C. M. Johnston, I. V. Zenyuk, *Adv. Energy Mater.* 2021, 11, 2101794.
- [17] S. Stariha, N. Macauley, B. T. Sneed, D. Langlois, K. L. More, R. Mukundan, R. L. Borup, *J. Electrochem. Soc.* 2018, 165, F492.
- [18] A. Kneer, N. Wagner, *J. Electrochem. Soc.* 2019, 166, F120.
- [19] D. Spermjak, R. Mukundan, R. L. Borup, L. G. Connolly, B. I. Zackin, V. D. Andrade, M. Wojcik, D. Y. Parkinson, D. L. Jacobson, D. S. Hussey, K. L. More, T. Chan, A. Z. Weber, I. V. Zenyuk, *ACS Appl. Energy Mater.* 2018, 1, 6006.
- [20] I. V. Zenyuk, R. Taspinar, A. R. Kalidindi, E. C. Kumbur, S. Litster, *J. Electrochem. Soc.* 2014, 161, F3091.
- [21] P. Satjaritanun, J. W. Weidner, S. Hirano, Z. Lu, Y. Khunatorn, S. Ogawa, S. E. Litster, A. D. Shum, I. V. Zenyuk, S. Shimpalee, *J. Electrochem. Soc.* 2017, 164, E3359.
- [22] T. A. Greszler, D. Caulk, P. Sinha, *J. Electrochem. Soc.* 2012, 159, F831.
- [23] J. A. Gilbert, N. N. Kariuki, X. Wang, A. J. Kropf, K. Yu, D. J. Groom, P. J. Ferreira, D. Morgan, D. J. Myers, *Electrochim. Acta* 2015, 173, 223.
- [24] A. Kneer, J. Jankovic, D. Susac, A. Putz, N. Wagner, M. Sabharwal, M. Secanell, *J. Electrochem. Soc.* 2018, 165, F3241.
- [25] C. Simon, F. Hasché, H. A. Gasteiger, *J. Electrochem. Soc.* 2017, 164, F591.
- [26] D. R. Baker, C. Wieser, K. C. Neyerlin, M. W. Murphy, *ECS Trans.* 2006, 3, 989.
- [27] A. D. Shum, D. Y. Parkinson, X. Xiao, A. Z. Weber, O. S. Burheim, I. V. Zenyuk, *Electrochim. Acta* 2017, 256, 279.
- [28] C. A. Schneider, W. S. Rasband, K. W. Eliceiri, *Nat. Methods* 2012, 9, 671.

- [29] S. Kabir, D. J. Myers, N. Kariuki, J. Park, G. Wang, A. Baker, N. Macauley, R. Mukundan, K. L. More, K. C. Neyerlin, *ACS Appl. Mater. Interfaces* **2019**, *11*, 45016.
- [30] F. De Carlo, D. Gursoy, F. Marone, M. Rivers, D. Y. Parkinson, F. Khan, N. Schwarz, D. J. Vine, S. Vogt, S-C. Gleber, S. Narayanan, M. Newville, T. Lanzirotti, Y. Sun, Y. P. Hong, C. Jacobsen, *J. Synchrotron Radiat.* **2014**, *21*, 1224.
- [31] L. Cheng, K. Khedekar, M. R. Talarposhti, A. Perego, M. Metzger, S. Kuppan, S. Stewart, P. Atanassov, N. Tamura, N. Craig, I. V. Zenyuk, C. M. Johnston, *Adv. Energy Mater.* **2020**, *10*, 2000623.